Modulated Model Predictive Control With Branch and Band Scheme for Unbalanced Load Compensation by MMCC-STATCOM

Xuejiao Pan, Li Zhang, *Senior Member, IEEE*, Yongfei Li, Kang Li, *Senior Member, IEEE*, and Han Huang, *Member, IEEE*

***Abstract*—This article presents a novel modulated model-predictive control (MMPC) scheme for modular multilevel cascaded converter-based static synchronous compensator (STATCOMs) (MMCC-STATCOMs) to compensate unbalanced load current and regulate reactive power flow. By adding a common-mode voltage (CMV) to the phase-voltages of the star-connected MMCC current model, the method allows natural injection of a nonsinusoidal voltage to the neutral point of the converter, hence achieving interphase cluster voltage balance. Moreover, the imposed CMV is shown to extend the operating ranges of MMCC-STATCOMs when used for negative sequence current compensation. The proposed MMPC method incorporates a modified branch and bound algorithm to optimize the per-phase switch duty ratios. It is shown to be computationally more efficient compared to model-predictive control schemes using the optimal voltage level method combined with voltage sorting schemes. Experimental results with different weighting factors confirm the effectiveness of this control scheme and compared favorably with the conventional scheme of injecting only a sinusoidal zero-sequence voltage.**

***Index Terms*—Branch and bound (B&B) method, modulated model-predictive control (MMPC), multilevel modular cascaded converter-based static synchronous compensator (STATCOM) (MMCC-STATCOM).**

I. Introduction

INCREASING use of power electronic driven loads, such as electric vehicles and electric traction, and rapid introduction of renewable energy sources in the power network, results in a growing incidence of reactive, unbalanced load current, and harmonics. The voltage-source-based static synchronous compensator (STATCOM) [1]–[3] can be effective in dealing with these problems, especially the unbalanced loads. STATCOM development has been furthered in the last decade by using modular multilevel cascaded converters (MMCCs), which extend the compensation applications to the medium and high-voltage power grids [4]–[6]. An MMCC-STATCOM can be scaled up to generate higher voltages without step-up transformers and can produce voltage waveforms with the good harmonic performance at lower switching frequencies and with less filtering. The key elements in an MMCC-STATCOM are its submodules (SMs), where the most widely used topology is the single-phase three-level H-bridge converter [7]. Other well-known topologies, such as five-level flying capacitor converter (5L-FC) [8] and five-level neutral point clamped converter [9], [10], have also been reported. Their relative merits have been investigated in terms of manufacturing cost, operational performance, and footprint [11].

A critical issue in using MMCC-STATCOMs for power quality control is maintaining the balance of module capacitor voltages. Lacking common dc-links, the capacitors in the cascaded modules are isolated from each other, making it difficult to exchange power between levels in the SM stack [12]–[14] and between the phase arms [15]–[17]. This causes module capacitor voltages to drift away from their nominal level, disrupting normal operation, or even causing device damage. This intracluster voltage imbalance can be counteracted within one phase arm by closed-loop average capacitor voltage control and adjustment of the pulsewidth modulation (PWM) schemes. However, when the MMCC-STATCOM compensates unbalanced loading of the utility grid, the module capacitor voltage imbalance can be worsened. This is due to STATCOM supplying negative sequence current to the grid for mitigating unbalanced loads, which causes active power imbalance between its phase arms. Countermeasures have been developed where, for the STAR-connected MMCC-STATCOM, the approach is to introduce a sinusoidal zero-sequence voltage at the neutral point, hence shifting the neutral point to a nonzero voltage level [18]–[22]. The effect of this is to eliminate the phase power differences caused by negative sequence current flowing through the phase arms, and bring about a uniform active power distribution between phases. However, such a scheme is problematic since the injected zero-sequence voltage can cause the converter phase voltages to exceed their rated levels under higher load imbalance, hence operating in overmodulation mode or even becoming uncontrollable. Methods, such as adding the third-order harmonics, can reduce the peak value of the zero-sequence voltage but with a limited effect. As shown in [23], the peak

Manuscript received June 29, 2021; revised September 25, 2021 and December 25, 2021; accepted February 10, 2022. Date of publication February 23, 2022; date of current version April 28, 2022. Recommended for publication by Associate Editor M. A. Perez. *(Corresponding author: Li Zhang.)*

Xuejiao Pan, Li Zhang, Yongfei Li, and Kang Li are with the School of Electrical Engineering, University of Leeds, LS2 9JT Leeds, U.K. (e-mail: ml16xp@leeds.ac.uk; l.zhang@leeds.ac.uk; elyli3@leeds.ac.uk; k.li1@leeds.ac.uk).

Han Huang is with the HVDC Center of Excellence, GE Renewable Energy, ST17 4DR Stafford, U.K. (e-mail: clanxyhuang@gmail.com).

Color versions of one or more figures in this article are available at https://doi.org/10.1109/TPEL.2022.3152407.

Digital Object Identifier 10.1109/TPEL.2022.3152407

phase-voltage reduction obtained is only about 12%, this has given an increased compensation range to the maximum load imbalance ratio from about 58% up to 65%. Injecting negative sequence voltage on the converter phase reference voltages has also been suggested to realize redistribution of phase active power in MMCC-STATCOM [24]–[26], but this is mainly for dealing with the condition of grid voltage sag. A technique using both negative-sequence current and zero-sequence voltage was also proposed for MMCC-STATCOM [27]. This is specifically for operating under power grid fault conditions but cannot cope with load imbalance.

The model predictive control (MPC) technique is well-known and has been widely applied for the control of modular multilevel converters, mostly for high-voltage direct current (HVdc) applications. In general, this method employs a discrete-time model of the MMCC circuit to predict the output phase current. It then selects the optimal switching state, which minimizes a desired cost function. The challenges of the technique can be the determination of the optimal switching state/vector from many candidates in real time. There are various schemes reported, which can be categorized into finite-control-set model predictive control [28]–[33] and the continuous control set model predictive control (CCS-MPC) method [34]–[38], which is also named as modulated model-predictive control (MMPC). The former relies on selecting a switching state from a finite set for the corresponding converter, combined with a sorting algorithm for balancing SMs capacitor voltages at the next switching cycle. This method has been applied to a wide range of power converters and shown giving high dynamic performance. However, its drawbacks are in giving variable switching frequency and poor steady-state performance because only one result can be output per sampling period [39]. The CCS-MPC, on the other hand, predicts the voltage control signals, which are continuous variables in one sample period and translate them into switching vectors. The method offers the benefit of causing smaller current ripples and requires less computational effort. In terms of implementing the predicted voltage, there is also the optimal voltage level-based-MPC [29], which uses a cost function similar to that in [28] but evaluates the desired number of SMs to be inserted or bypassed in each phase arm. In addition, Liu *et al.* [30] proposed a combined grouping and sorting optimal MPC for MMC HVdc, which divides n SMs in each arm into m groups. By implementing optimized MPC at group level and then SM level, the method can further reduce the computational burden. There is also a dual-stage-based MPC [31], where the first stage aims to obtain the optimal voltage level and the second to select the switching states using another MPC without the sorting algorithm. For modulation techniques, space vector modulation scheme is utilized for MMC applications [36], [37] to enhance the steady-state performance with fixed switching frequency. The optimal times for three active vectors (two active vectors and one zero vector) need to be calculated for minimizing the cost function value. Different sine-triangle-based PWM techniques are also adopted in [38] for voltage source inverters. These give the performance similar to that from the space-vector-based modulation scheme but can further simplify the computational burden. In particular, the phase-shift PWM (PS-PWM) is the most popular for its advantage in maintaining SM voltage balance [35]

There are only a few MPC schemes dedicated to MMCC-STATCOMs [40]–[42], but they all concentrate on compensating reactive power under balanced grid operation; none is for compensating unbalance load current. The proposed MMPC method in this article focuses on suppressing the grid unbalanced load current. It has two distinctive features; first, the three-phase voltages applied to its model for current prediction are imposed with a common-mode voltage (CMV). This gives the implemented phase voltages a natural zero-sequence element with harmonics for bringing symmetry to the phase active powers, and hence, eliminating drift in the phase cluster voltages. Moreover, the harmonics in the imposed CMV are found to reduce the peak converter phase voltages, so extending the range of load imbalance compensation. Second, the cost function minimization is achieved by selecting the per phase switch duty ratio using a modified branch and bound (B&B) algorithm. This approach stems from the scheme in [40], which applies the space vector PWM concept and selects the switching vectors within each 60° sextant. The modified B&B, however, evaluates the optimal switch duty ratios in $a-b-c$ coordinate. By setting any one of them in the cost function as a branch, it solves the other two by quadratic programming. It will be shown that the method is able to mitigate unbalance load at the ratio up to 70% while still maintaining the phase dc-voltages balance.

The rest of this article is organized as follows. Section II describes the configuration of the MMCC-STATCOM and prediction models for output current and per phase dc capacitor voltage. In Section III, the cost function and constraints for the variables are defined. The principle of the modified B&B method is detailed. In Section IV, the overall control scheme is presented. Section VI presents the experimental results, which validate the proposed control scheme. Finally, Section VII concludes this article.

II. MMPC With Common Voltage Injection

A. Configuration of MMCC-STATCOM

The configuration of a STAR-connected MMCC-STATCOM is shown in Fig. 1. Each of the three-phase arms consists of M serially connected five-level flying capacitor converters as SM, which has two inner capacitors C_1 and C_2 and one outer floating capacitor C_3. The SMs can equally be two-level full-bridge converters, each with a single capacitor. Each of the flying capacitor SMs can synthesize five voltage level: 0, $\pm V_{\rm dc}/2$, $\pm V_{\rm dc}$. With M SM per phase arm, there are $4M+1$ voltage levels. The number of SMs in a phase arm depends on the line voltage rating and dc capacitor voltage per module. The three-phase arms are connected to the transmission lines through their filters with impedance R_f+jwL_f, to Bus2, which is regarded as the point of common coupling (PCC). The transmission line impedance between the supply source at Bus1 to Bus2 is R_s+jwL_s. The neutral points between the supply and converter sides are not connected [23].

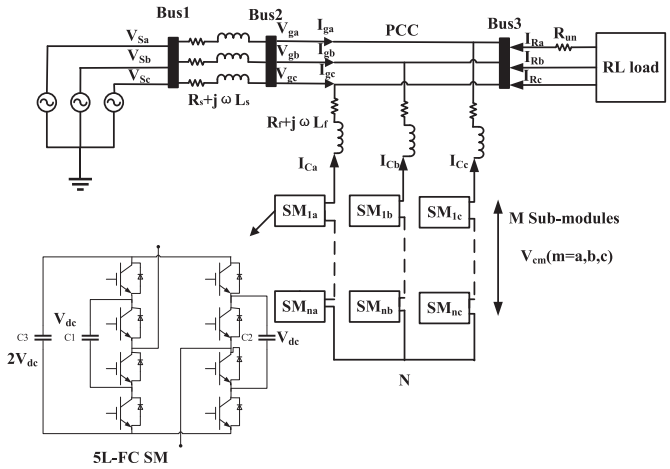

Fig. 1. Configuration of a power system with the STAR-connected MMCC-STATCOM using five-level flying capacitor converter as SMs.

At the load end, three-phase $R-L$ loads, R_L+jwL_L is connected. Its power factor is about 80.9%. To emulate load imbalance condition, a single-phase variable resistor, R_{un} is added on the load of phase A.

B. Model for STATCOM Output Current

The MMCC-STATCOM is used to compensate the unbalanced load current as well as the reactive power within its rated power and voltage ratings. This has the benefit of making the current flow from PCC balanced, hence eliminating the adverse effect due to load imbalance to the grid. However, supplying unbalanced current by an MMCC-STATCOM causes phase power imbalance, resulting, consequently, phase cluster dc voltages drifting away from the nominal level. The existing technique is to inject a zero-sequence voltage, which would not affect the grid voltage but results in a power element eliminating the unbalanced power between phases, hence preventing phase voltage drift. To adapt the new approach, it is assumed a CMV, equivalent to the zero-sequence voltage at the fundamental frequency, is applied to the neutral point of the STAR-connected STATCOM. By applying the phase voltage balance expression, the rate of change of per phase current of the converter can be given as

$$\frac{dI_{\text{cm}}}{dt} = \frac{1}{L_f} \times (V_{\text{cm}} - V_{\text{gm}} + V_{n0} - R_f I_{\text{cm}}) \tag{1}$$

where V_{cm} and I_{cm} $(m = a, b, c)$ are, respectively, the STATCOM terminal voltage and current, while V_{gm} is the grid side voltage, and V_{n0} is the CMV, which can be expressed as

$$V_{n0} = -\frac{V_{ca} + V_{cb} + V_{cc}}{3}. \tag{2}$$

Assuming that the sample time T_s is significantly smaller than the time constant of the converter filter, if the converter three phase-voltages and the CMV at the kth sample are known. The discrete-time expression of output three phase-currents at the $(k+1)$th sample can be given as

$$\begin{bmatrix} I_{ca}(k+1)) \\ I_{cb}(k+1)) \\ I_{cc}(k+1)) \end{bmatrix} = \frac{T_s}{L_f} \begin{bmatrix} V_{ca}(k)) \\ V_{cb}(k)) \\ V_{cc}(k)) \end{bmatrix} - \frac{T_s}{L_f} \begin{bmatrix} V_{ga}(k)) \\ V_{gb}(k)) \\ V_{gc}(k)) \end{bmatrix} + \frac{T_s}{L_f} \begin{bmatrix} V_{no}(k)) \\ V_{no}(k) \\ V_{no}(k) \end{bmatrix} + \left(1 - \frac{R_f T_s}{L_f}\right) \begin{bmatrix} I_{ca}(k)) \\ I_{cb}(k)) \\ I_{cc}(k)) \end{bmatrix}. \tag{3}$$

Considering the converter phase voltage V_{cm}, its maximum value equals the sum of voltages of all SMs in a phase chain, assuming that V_m^{Σ} is the sum value of SM capacitor voltages. Applying switch duty ratio, V_{cm} relates to V_m^{Σ} and S_m as

$$V_{\text{cm}} = S_m V_m^{\Sigma} \tag{4}$$

where S_m is the duty ratio for each phase $(m = a, b, c)$ and M is the number of SM per phase arm. Since the duty ratio varies at every sample interval, the discrete time form of CMV is given as

$$V_{n0}(k) = -\frac{\left(S_a(k)V_a^{\Sigma}(k) + S_b(k)V_b^{\Sigma}(k) + S_c(k)V_c^{\Sigma}(k)\right)}{3}. \tag{5}$$

Substituting (5) into (3), the STATCOM current at $(k+1)$th sample can be expressed as

$$\begin{bmatrix} I_{ca}(k+1)) \\ I_{cb}(k+1)) \\ I_{cc}(k+1)) \end{bmatrix} = \frac{T_s}{L_f} \begin{bmatrix} \frac{2}{3} & -\frac{1}{3} & -\frac{1}{3} \\ -\frac{1}{3} & \frac{2}{3} & -\frac{1}{3} \\ -\frac{1}{3} & -\frac{1}{3} & \frac{2}{3} \end{bmatrix} \begin{bmatrix} S_a(k)V_a^{\Sigma}(k) \\ S_b(k)V_b^{\Sigma}(k) \\ S_c(k)V_c^{\Sigma}(k) \end{bmatrix} - \frac{T_s}{L_f} \begin{bmatrix} V_{ga}(k)) \\ V_{gb}(k)) \\ V_{gc}(k)) \end{bmatrix} + \left(1 - \frac{R_f T_s}{L_f}\right) \begin{bmatrix} I_{ca}(k)) \\ I_{cb}(k)) \\ I_{cc}(k)) \end{bmatrix}. \tag{6}$$

Assuming filter parameters, L_f and R_f are constant and $V_m^{\Sigma}(k)$, $V_{\text{gm}}(k)$, and $I_{\text{cm}}(k)$ $(m = a, b, c)$ are the measured values at the kth sample, by adequately adjusting $S_m(k)$, it is possible to obtain desired STATCOM current at the $(k+1)$th sample.

C. Model for Per Phase Voltage

The power flow between the grid and MMCC-STATCOM maintains SM capacitor voltages at the desired levels; hence, the energy exchange per STATCOM phase arm can be given as

$$\frac{1}{2}C \begin{bmatrix} V_a^{\Sigma 2} \\ V_b^{\Sigma 2} \\ V_c^{\Sigma 2} \end{bmatrix} = \int \left(\begin{bmatrix} -V_{ca} I_{ca} \\ -V_{cb} I_{cb} \\ -V_{cc} I_{cc} \end{bmatrix} \right) dt \tag{7}$$

where C is the capacitance of the SM outer floating capacitor C_3.

According to (4), the above-mentioned can be written as

$$\frac{1}{2}C \begin{bmatrix} V_a^{\Sigma 2} \\ V_b^{\Sigma 2} \\ V_c^{\Sigma 2} \end{bmatrix} = -\int \left(\begin{bmatrix} S_a V_a^{\Sigma} I_{ca} \\ S_b V_b^{\Sigma} I_{cb} \\ S_c V_c^{\Sigma} I_{cc} \end{bmatrix} \right) dt. \tag{8}$$

Taking derivative on both side and simplifying the resultant formula, the rate of change of per phase total capacitor voltage is given by

$$\frac{d\begin{bmatrix}V_a^{\Sigma}\\V_b^{\Sigma}\\V_c^{\Sigma}\end{bmatrix}}{dt}=-\frac{1}{C}\begin{bmatrix}S_aI_{ca}\\S_bI_{cb}\\S_cI_{cc}\end{bmatrix}. \tag{9}$$

Expressing above-mentioned in the discrete-time form, the MMCC-STATCOM phase arm total voltages at the next sample interval can be expressed as

$$\begin{bmatrix}V_a^{\Sigma}(k+1)\\V_b^{\Sigma}(k+1)\\V_c^{\Sigma}(k+1)\end{bmatrix}=-\frac{T_s}{C}\begin{bmatrix}S_a(k)I_{ca}(k)\\S_b(k)I_{cb}(k)\\S_c(k)I_{cc}(k)\end{bmatrix}+\begin{bmatrix}V_a^{\Sigma}(k)\\V_b^{\Sigma}(k)\\V_c^{\Sigma}(k)\end{bmatrix}. \tag{10}$$

It is evident from (10) that the total phase voltage of STATCOM is also adjustable by the switch duty ration of phase arm SMs.

III. MMPC FOR MMCC-STATCOM

A. Cost Function and Constrained Optimization Principle

In this section, an MMPC method based on the $a-b-c$ framework with CMV injection is given in details. The control objective is to ensure that three phase currents of the MMCC-STATCOM track as well as possible their corresponding reference values while the fluctuations on the sum of SM capacitor voltages per phase are minimized. This can be achieved by evaluating the optimal control variables, i.e., the switch duty ratio $S_m(k)$. However, it is worth noting that with the current reference values defined to compensate the unbalanced load current at PCC, a CMV is imposed on each phase voltage and this may result in any one of the optimal duty ratios exceeding outside the linear modulation range, causing MMCC overmodulation. Thus, a cost function combining both current and voltage objectives, with the constraints on $S_m(k)$, is defined as

$$\begin{aligned}J(k)=&\sum_{m=a,b,c}\left\{\left(I_{\text{cm}}(k+1)-I_{\text{cm}}^{*}(k+1)\right)^2\right\}\\&+\lambda\sum_{m=a,b,c}\left\{\left(V_m^{\Sigma}(k+1)-V_m^{\Sigma *}(k+1)\right)^2\right\}\\&\text{s.t.}\,|S_m(k)|\le 1\end{aligned} \tag{11}$$

where $I_{\text{cm}}^{*}(k+1)$ and $V_m^{\Sigma *}(k+1)$ are the reference values of converter current and sum of capacitor voltages per phase. λ is the weighting factor for capacitor voltage balancing. The constraints on per phase switch duty ratio ensure that the voltage variations are within the linear range.

The weighting factor λ imposes a tradeoff between the current tracking accuracy and balancing of three summed SM capacitor voltages. Its value is determined by trial and error. A comparative study of using different λ in the control of the experimental rig is presented in Section V and, subsequently, the selection of its value is explained.

Without considering CMV in the cost function, the optimization method can be very similar to that presented in [43]. However, with the addition of CMV on each of the phase voltages, the expressions for the three-phase currents are different as shown in (6), so minimization of cost function (11) for finding the three voltage duty ratios requires considering all three-phase current simultaneously under inequality constraints. Applying the Karush–Kuhn–Tucker (KKT) conditions [44] gives a set of sufficient conditions for optimizing the cost function (11), this leads to the constraints for the three duty ratios written as

$$\text{s.t.}\,-1-S_m(k)\le 0, S_m(k)-1\le 0 (m=a,b,c). \tag{12}$$

Subsequently according to KKT, the Lagrarian function of (11) combining with (12) can be shown as

$$\begin{aligned}L(k,\lambda_1,\lambda_2,\lambda_3,\lambda_4,\lambda_5,\lambda_6)=&J(k)+\lambda_1(-1-S_a(k))\\&+\lambda_2(S_a(k)-1)+\lambda_3(-1-S_b(k))+\lambda_4(S_b(k)-1)\\&+\lambda_5(-1-S_c(k))+\lambda_6(S_c(k)-1).\end{aligned} \tag{13}$$

Taking phase a as an example, the errors of both current prediction and capacitor voltage balance are simplified, respectively, as

$$\begin{aligned}I_{ca}(k+1)-I_{ca}^{*}(k+1)&=a_1S_a(k)+a_2S_b(k)+P_{a1}\\V_a^{\Sigma}(k+1)-V_a^{\Sigma *}(k+1)&=a_4S_a(k)+P_{a2}\end{aligned} \tag{14}$$

where

$$a_1=\frac{2}{3}\frac{T_s}{L_f}V_a^{\Sigma}(k), a_2=-\frac{1}{3}\frac{T_s}{L_f}V_b^{\Sigma}(k)$$

$$a_3=-\frac{1}{3}\frac{T_s}{L_f}V_c^{\Sigma}(k), a_4=-\frac{T_s}{C}I_{ca}(k)$$

$$P_{a1}=-\frac{T_s}{L_f}V_{ga}(k)+\left(1-\frac{R_fT_s}{L_f}\right)I_{ca}(k)-I_{ca}^{*}(k+1)$$

$$P_{a2}=V_a^{\Sigma}(k)-V_a^{\Sigma *}(k+1).$$

Subsequently the $J(k)$ part in Lagrarian function (3) can be rewritten as

$$\begin{aligned}J(k)=&\sum_{m=a,b,c}\left\{\left(m_1S_a(k)+m_2S_b(k)+m_3S_c(k)+P_{m1}\right)^2\right\}\\&+\lambda\sum_{m=a,b,c}\left\{\left(m_4S_m(k)+P_{m2}\right)^2\right\}.\end{aligned} \tag{15}$$

Note that the parameters, m_1, m_2, m_3, and P_{m1}, P_{m2} in (15) are given in the Appendix. Hence, KKT conditions that need to be met are as follows:

$$\begin{aligned}\frac{\partial L}{\partial S_a(k)}=&(a_1^2+b_1^2+c_1^2+\lambda a_4^2)\times S_a(k)+(a_1a_2+b_1b_2\\&+c_1c_2)\times S_b(k)+(a_1a_3+b_1b_3+c_1c_3)\times S_c(k)\\&+(a_1P_{a1}+b_1P_{b1}+c_1P_{c1}+\lambda a_4P_{a2})-\lambda_1+\lambda_2=0\\\frac{\partial L}{\partial S_b(k)}=&(a_1a_2+b_1b_2+c_1c_2)\times S_a(k)+(a_2^2+b_2^2+c_2^2\\&+\lambda b_4^2)\times S_b(k)+(a_2a_3+b_2b_3+c_2c_3)\times S_c(k)\end{aligned}$$

$$+ (a_2P_{a1} + b_2P_{b1} + c_2P_{c1} + \lambda b_4P_{b2}) - \lambda_3 + \lambda_4 = 0$$

$$\frac{\partial L}{\partial S_c(k)} = (a_3a_1 + b_3b_1 + c_3c_1) \times S_a(k) + (a_3a_2 + b_3b_2 + c_3c_2) \times S_b(k) + (a_3^2 + b_3^2 + c_3^2 + \lambda c_4^2) \times S_c(k) + (a_3P_{a1} + b_3P_{b1} + c_3P_{c1} + \lambda c_4P_{b2}) - \lambda_5 + \lambda_6 = 0$$

$$-1 - S_a(k) \le 0, S_a(k) - 1 \le 0, -1 - S_b(k) \le 0$$

$$S_b(k) - 1 \le 0, -1 - S_c(k) \le 0, S_c(k) - 1 \le 0$$

$$\lambda_1(-1 - S_a(k)) = 0, \lambda_2(S_a(k) - 1) = 0, \lambda_3(-1 - S_b(k)) = 0$$

$$\lambda_4(S_b(k) - 1) = 0, \lambda_5(-1 - S_c(k)) = 0, \lambda_6(S_c(k) - 1) = 0$$

$$\lambda_1 \ge 0, \lambda_2 \ge 0, \lambda_3 \ge 0, \lambda_4 \ge 0, \lambda_5 \ge 0, \lambda_6 \ge 0. \quad (16)$$

Solving the above-mentioned equations with the set conditions leads to the derivations of the values $S_m(k)(m = a, b, c)$ and λs. If one of the λs is greater than 0, the corresponding phase duty ratio should be on the boundary 1 or −1. On the other hand, when λ is equal to 0, the derived duty ratio is the optimal value. Several optimization methods may be applied to solve this problem, including interior-point (IP) [45] and active-set [43] schemes. They all require performing multiple iterative procedures, which can be computationally costly. A modified B&B is, thus, proposed, which can derive the optimal solution with only a finite known number of steps.

B. Modified B&B Method

To evaluate the optimal switch duty ratios $S_m(k)$ $(m = a, b, c)$ for minimizing the cost function defined by (11), a modified B&B method for system represented by $a - b - c$ coordinate is proposed.

The principle of the method is as follows. By selecting any one of the three control variables, namely, one phase arm's switch duty ratio and setting it variable within the confined range imposed by the constraint in the cost function, the cost function would now have only two variables-two switch duty ratios, as the third one is bounded as a constant. This simplifies the computation process because the order of the derived formula for cost function minimization is reduced to two other than the original three. The evaluation follows a two stage bound and branch process as follows.

Stage 1: The chosen input variable is assigned to a constant within its constraint from either the lower or upper boundary. With the cost function having now two independent variables, their optimal values can be estimated by quadratic programming.

Stage 2: The two resultant optimal values are applied to replace their originals as fixed constants in the cost function, but the first input is allowed us to vary. Having only one independent variable to evaluate, the optimal cost function can be derived subsequently. This, consequently, leads to a set of three optimal inputs and completes one branch of the B&B process.

In the following branches, the first input variable ascends or descends in constant steps until it reaches the upmost/lowest boundary. In each step, the two-stage process described earlier is repeated. According to the number of steps taken by the chosen first variable, there would be multiple branches, hence, multiple sets of results. These results are compared after completing the final branch evaluation and the set giving the minimum cost function value will be chosen.

Applying the above-mentioned principle, the switch duty ratio, $S_c(k)$, in the cost function (11) may be the chosen one amongst the three to form a branch. Starting from $S_c(k) = -1$ at the lower bound, S_L, it rises at a constant step size of, say, 0.25, in each branch until reaching to the upmost bound S_U=1. By setting S_c as a constant in the cost function (11) in each branch, the current prediction error part is simplified as given below (taking phase a as an example)

$$I_{ca}(k+1) - I_{ca}^*(k+1) = a_1S_a(k) + a_2S_b(k) + n_{a1} \quad (17)$$

where

$$n_{a1} = a_3S_c(k) - \frac{T_s}{L_f}V_{ga}(k) + \left(1 - \frac{R_fT_s}{L_f}\right) I_{ca}(k) - I_{ca}^*(k+1).$$

Likewise combining (17), the phase A voltage error can be expressed as

$$V_a^{\Sigma}(k+1) - V_a^{\Sigma *}(k+1) = a_4S_a(k) + n_{a2} \quad (18)$$

where

$$n_{a2} = V_a^{\Sigma}(k) - V_a^{\Sigma *}(k+1).$$

Subsequently, the cost function (11) can be rewritten as

$$J(k) = \sum_{m=a,b,c} \left\{ (m_1S_a(k) + m_2S_b(k) + n_{m1})^2 \right\} + \lambda \sum_{m=a,b,c} \left\{ (m_4S_m(k) + n_{m2})^2 \right\}. \quad (19)$$

Note that the parameters, m_1, m_2, and n_{m1}, n_{m2} in the original (15) and (19) are given in the Appendix. With only $S_a(k)$ and $S_b(k)$ as the input variables, the optimal values of these parameters are obtainable by minimizing the cost function $J(S_a, S_b)$ and can be estimated using the least-square minimization algorithm. This requires taking the first-order derivatives of the cost function J with respect to the two variables, respectively, and setting them to zero, yielding

$$\frac{\partial J(k)}{\partial S_a(k)} = (a_1^2 + b_1^2 + c_1^2 + \lambda a_4^2) \times S_a(k) + (a_1a_2 + b_1b_2 + c_1c_2) \times S_b(k) + (a_1n_{a1} + bn_{b1} + c_1n_{c1} + \lambda a_4n_{a2}) = 0 \quad (20)$$

$$\frac{\partial J(k)}{\partial S_b(k)} = (a_1a_2 + b_1b_2 + c_1c_2) \times S_a(k) + (a_2^2 + b_2^2 + c_2^2 + \lambda b_4^2) \times S_b(k) + (a_2n_{a1} + b_2n_{b1} + c_2n_{c1} + \lambda b_4n_{b2}) = 0. \quad (21)$$

Based on the above-mentioned equations, the solutions for the two switching duty ratios can be obtained by the product of

two 2×2 matrices as shown in the following:

$$\begin{bmatrix} S_a(k) \\ S_b(k) \end{bmatrix} = -A_1^{-1} A_2 \tag{22}$$

where $A_1 = \begin{bmatrix} a_1^2 + b_1^2 + c_1^2 + \lambda a_4^2 & a_1a_2 + b_1b_2 + c_1c_2 \\ a_1a_2 + b_1b_2 + c_1c_2 & a_2^2 + b_2^2 + c_2^2 + \lambda b_4^2 \end{bmatrix}$ and $A_2 = \begin{bmatrix} a_1n_{a1} + b_1n_{b1} + c_1n_{c1} + \lambda a_4n_{a2} \\ a_2n_{a1} + b_2n_{b1} + c_2n_{c1} + \lambda b_4n_{b2} \end{bmatrix}$.

Note that either $S_a(k)$ or $S_b(k)$ estimated from (22) may violate the constraint defined in (11), and in that case, the corresponding duty ratio needs to be clamped to its nearest boundary value.

Once the optimal $S_a(k)$ and $S_b(k)$ are obtained with a fixed $S_c(k)$, the next stage is to estimate the optimal duty ratio $S_c(k)$ while $S_a(k)$ and $S_b(k)$ in (11) are fixed to their newly evaluated values. In this case, $S_c(k)$ is the only parameter to be evaluated, and this is a one-variable programming problem. The cost function (11) now become

$$J(k) = \sum_{m=a,b,c} \left\{ (m_3 S_c(k) + n_{m3})^2 \right\} + \lambda \sum_{m=a,b,c} \left\{ (m_4 S_m(k) + n_{m2})^2 \right\} \tag{23}$$

where

$$n_{m3} = m_1 S_a(k) + m_2 S_b(k) - \frac{T_s}{L_f} V_{\text{gm}}(k) + \left(1 - \frac{R_f T_s}{L_f}\right) I_{\text{cm}}(k) - I^*_{\text{cm}}(k+1).$$

Taking derivative of $J(S_c(k))$ with respect to $S_c(k)$ and setting it to 0, $S_c(k)$ is calculated as

$$S_c(k) = -\frac{a_3n_{a3} + b_3n_{b3} + c_3n_{c3} + \lambda c_4 n_{c2}}{a_3^2 + b_3^2 + c_3^2 + \lambda c_4^2} \tag{24}$$

where $a_3, b_3, c_3, n_{a3}, n_{b3}$, and n_{c3} are also shown in the Appendix.

Similar to the case with the estimated $S_a(k)$ and $S_b(k)$, the derived $S_c(k)$ value should not violate the set constraint, otherwise it must also be replaced with the nearest boundary value.

The switch duty ratio values for three-phase arms estimated using the aforementioned procedure may not be the global optimum. The optimization process is repeated for the next branch in which $S_c(k)$ is fixed to a value higher or lower than its previously acquired value. With the defined constraint for the switch duty ratio and the step size setting of 0.25, there are nine branches, resulting in nine sets of optimal solutions. Based on their corresponding cost function values, the one producing the minimal value among the nine sets is selected. The flowchart of this new B&B method is shown in Fig. 2.

It is worth noting that the branch step size of 0.25 is set by trial and error according to the criteria of both the accuracy of the final optimal solution and computation efficiency. In general the smaller the step size, the more accurate the solution obtained according to the minimum cost function value, however, the higher the number of the branches and, hence, the higher the computational burden. Fig. 3 depicts the cost function values evaluated using the global optimal solution obtained when different step sizes are applied; i.e., 0.5(black line), 0.25(red line), and 0.1(blue line), respectively, and the unbalanced load ratio

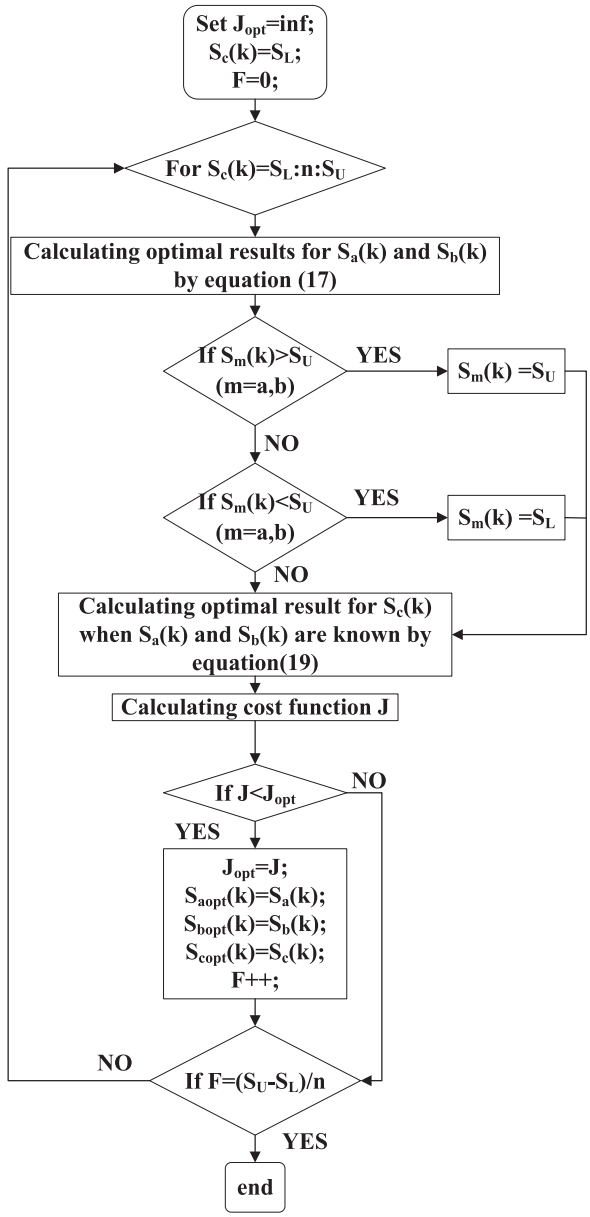

Fig. 2. Flowchart for modified B&B method.

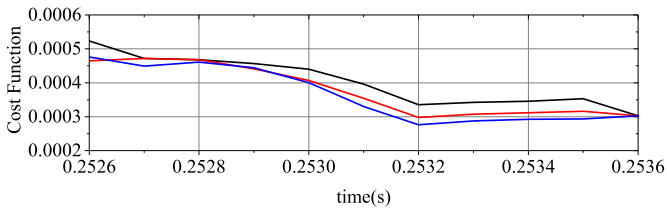

Fig. 3. Cost function value comparison using different step size when imbalance compensation ratio is 0.28.

TABLE I
PHASE DUTY RATIOS AND COST FUNCTION VALUES EVALUATED AT NINE DIFFERENT BRANCHES BY B&B METHOD AND RESULTS FROM IP METHOD

Branch	$S_a(k)$	$S_b(k)$	$S_c(k)$	Cost function value
S_c=-1	-0.6227	-1	-0.63434	1.329
S_c=-0.75	-1	-0.5085	-0.3733	0.6088
S_c=-0.5	-0.1240	-1	-0.3733	0.1833
S_c=-0.25	0.1154	-0.9964	-0.2519	0.05054
S_c=0	0.3748	-0.7377	-0.0022	0.05527
S_c=0.25	-0.4889	0.2476	0.6242	0.05828
S_c=0.5	0.8736	-0.2402	0.4974	0.06158
S_c=0.75	1	0.0856	0.6856	0.1
S_c=1	1	0.2573	0.8105	0.3974
Optimal value	0.1078	-1	-0.2720	0.04178

TABLE II
COMPARISON OF DUTY RATIOS AND COST FUNCTION VALUES ESTIMATED BY B&B METHOD AND IP METHOD AT FOUR DIFFERENT SAMPLES

Sample		$S_a(k)$	$S_b(k)$	$S_c(k)$	Cost function value	Cost function error
1	B&B	-0.2886	0.0816	0.7502	0.01096	0.00651
	IP	-0.2111	0.0875	0.8252	0.00445	
2	B&B	-0.5592	-0.1340	0.4999	0.02989	0.0084
	IP	-0.5026	-0.0983	0.5545	0.02149	
3	B&B	0.2926	0.2301	-0.1950	0.01831	0.00358
	IP	0.3084	0.2054	-0.2145	0.01473	
4	B&B	0.3513	-0.7843	-0.2506	0.00370	0.00255
	IP	0.2933	-0.8007	-0.2659	0.00115	
Average error		0.0482	0.0432	0.0411		0.00526

is 0.28. With only five branches for 0.5 step size, the black line either coincides with the other two lines or is higher than them. It can be seen that when the red line is higher than the blue line, the gap between them is not very obvious. However, 21 branches with 0.1 step size results in the computational time twice of that when step size is 0.25. Thus, in this article, a step size of 0.25, is chosen for each branch which is a compromised choice between accuracy and computational cost.

C. Results From B&B Compared With IP Method

It is important to note that the proposed B&B with step size set to 0.25 does not prevent it from estimating the optimal solution values. Table I illustrates evaluated optimal results for a single instance of a real time sample. It lists the three duty ratios at each of nine bounds and the final chosen result (shown in bold) having the lowest cost function of all those obtained for this particular test. Clearly, the evaluated three duty ratios vary over the constrained range and importantly, the final optimal solution chosen is compared with the result obtained by the IP method [46], the difference in terms of the cost functions between the two method are about 10% and the maximum difference between the estimated three duty ratios are less than 0.02. This is deemed to be a practically acceptable result, and is obtained much more rapidly than the IP method solution.

Results from both B&B and IP methods are also shown in Table II for four further instances, i.e., for four other time instants under different operating conditions. The figures listed in Table II presents a similar pattern to those in Table I, the maximum average difference in three duty ratios identified by two methods are less than 0.05, so helping to confirm robust results in the presence of noise, and sampling errors. In fact about 100 similar instances were analyzed but cannot be listed in full. All the results have been found to be acceptably close to those from the IP method. It is also worth pointing out that no instances of local minimum (i.e., in a region disjoint from the true optimum) were seen to occur.

TABLE III
EXPECTED BASIC OPERATIONS OF THE PROPOSED METHOD

Basic operations	Pre-calculation	Per cycle calculation
Addition	24	23
Multiplication	38	43
Comparison	0	6
Division	0	3
Square	0	6

TABLE IV
EXPECTED BASIC OPERATIONS OF THE CONVENTIONAL METHOD

Basic operations	Pre-calculation	Outer capacitor balancing control	Per cycle calculation
Addition	16	41	19
Multiplication	30	54	39
Comparison	0	0	6
Division	0	3	3
Square	0	0	6

D. Evaluation and Comparison of Computational Cost

Evaluations of the computational procedures are performed on both the proposed and conventional methods. To give a fair comparison, the MMPC method is also applied to the conventional method. The basic operations for both methods are, respectively, listed in Tables III and IV, including comparison, addition, multiplication, and division, performed per sample interval. The operations which are common to both methods, such as DDSRF, average voltage control loop and PS-PWM are excluded. There is a column in both tables named precalculation; this counts for computations not performed in each sample interval. It can be seen that the count for total basic operations for the proposed method is 791, which is less than that for conventional method of 801.

IV. OVERALL CONTROL SCHEME

The overall MMPC control scheme for an MMCC-SATCOM is shown in Fig. 4. It has the following four parts: MMPC block, phase-shifted PWM block, intracluster voltage balancing control block, reference current, and voltage generations and delay compensator. MMPC block is already described in Section III. The phase-shifted PWM (PS-PWM) block is well-reported in the literature, and hence, only a brief description is given here [47]. In this technique, multiple triangular carrier waves are applied to synthesize a three-phase sinusoidal reference signal. The number of triangular waves is the number of SMs (for SM being full H-bridge), in the case of 5L-FL SMs, the number is twice that of the SMs in a phase leg. Thus, with the number being M,

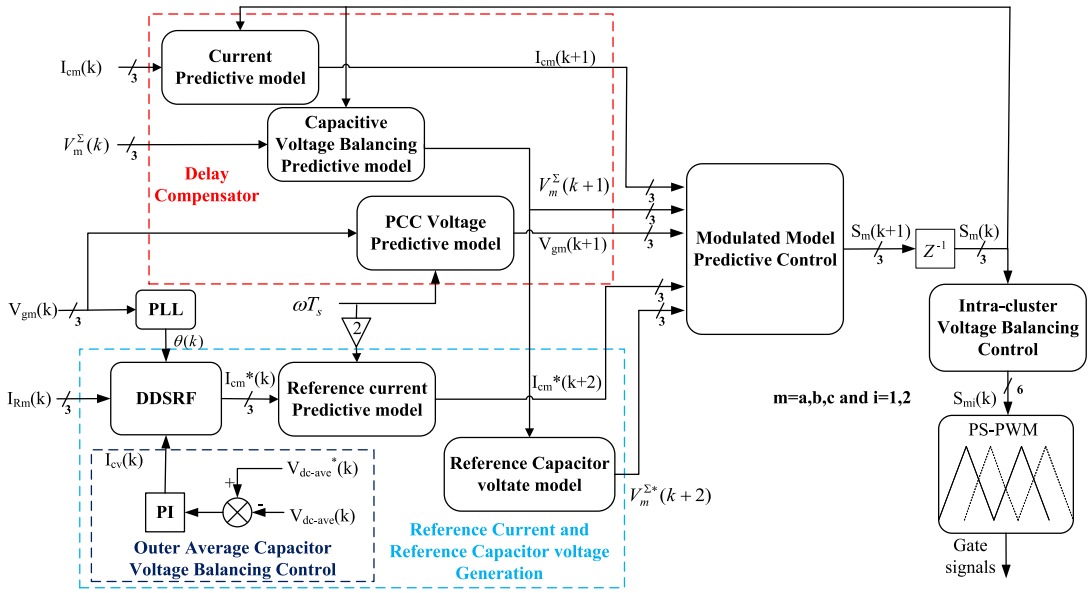

Fig. 4. Overall control scheme of MMPC for MMCC-STATCOM.

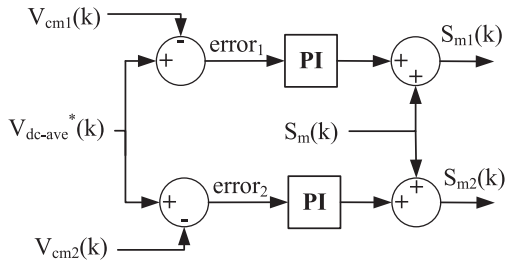

Fig. 5. Diagram for intracluster voltage balancing control block.

they are phase shifted by an equal angle $((180/2\,M)^\circ)$ to each other. By comparing these carrier waves with two antiphased reference sine waves, desired switching signals can be generated. In the intracluster voltage balancing control block, the per phase SM capacitor voltage values, i.e., the intraphase voltages, are maintained in balance by using closed-loop control to their average value $v^*_{\text{dc-ave}} = v^{\Sigma}_m/M$ and then applying PS-PWM, which has been shown in Fig. 5. V_{cm1} and V_{cm2} represent the voltage values of two SM outer capacitors, C_3, in each phase $(m = a, b, c)$. The last two blocks are described in details as follows.

A. Reference Current and Voltage Generations

For MMPC+B&B scheme to eliminate the unbalance current and improve the power factor at PCC, its reference current $I^*_{\text{cm}}(k)$, is generated by extracting both the $-ve$ sequence current components, $I^-_{1\,d}(k)$, $I^-_{1q}(k)$, and reactive current $I^+_{1q}(k)$ from the measured load current. This can be achieved by using the decoupled double synchronization reference frame (DDSRF) [48]. For intracluster voltage balancing, a +ve sequence current element $I_{\text{cv}}(k)$ needs to be added to the reference current. This is evaluated using the SM average voltage control block as shown in Fig. 5. Subsequently, the reference current generated consists of $I^-_{1\,d}(k)$+$I_{\text{cv}}(k)$ and $I_{1q}(k)$. This is transformed to the $a-b-c$ stationary reference frame through inverse Park transformation, hence, given as, $I^*_{\text{cm}}(k)$.

For good performance control, the delay compensation, explained in the following section, is applied. In this reference current at the $(k+2)$th sample, $I^*_{\text{cm}}(k+2)$, is estimated by multiplying $I^*_{\text{cm}}(k)$ with $B(2\sigma)$, which is expressed in (26).

With the delay compensator inserted, the average phase arm reference voltage value for the $(k+2)$th sample should be evaluated according to their corresponding predicted values at the $(k+1)$ sample instant as

$$V^{\Sigma *}_m(k+2) = (V^{\Sigma}_a(k+1) + V^{\Sigma}_b(k+1) + V^{\Sigma}_c(k+1))/3. \tag{25}$$

B. Delay Compensator

As elaborated in the previous section, the MMPC with the modified B&B algorithm predicts the converter output current and SM capacitor voltages, and estimates the optimal switching duty ratios for all three-phase arms in nine calculation branches. The whole process is, however, complicated, making the time interval excessively long between the time instant taking the measured voltage and current at the kth sample and the instant of when the newly estimated switching signals are obtained. This is called the digital control delay and may cause inaccurate predictions of current and voltage, hence, a poor control performance. In this article, a delay compensator is implemented to tackle this problem. Its effect is analogues to inserting a "state observer" for current and SM capacitor voltages in the MMPC loop. The scheme takes the measured converter current and capacitor voltages at the kth sample and applies the switch duty ratios, $S_m(k)$, to (6) and (10), to predict $I_{\text{cm}}(k+1)$, and the sum of phase capacitor voltages, $V^{\Sigma}_m(k+1)$. It also estimates the $(k+1)$th PCC voltages, $V_{\text{gm}}(k+1)$, expressed in the $a-b-c$

TABLE V
PARAMETERS FOR EXPERIMENTAL RIG

Rated Power P_norm	1.5kVA
Rated Current I_norm	5A
Sending end voltage V_s	80V
Line frequency f	50Hz
RL filter resistance R_f	2Ω
RL filter inductance L_f	3mH
Flying capacitor SM per per phase cluster M	2
Per Module Capacitor C_3	1120μF
Inner capacitor C_1 and C_2	560μF
Per Module voltage	60V
Switching frequency	1kHz

coordinate as

$$\begin{bmatrix} V_{ga}(k+1) \\ V_{gb}(k+1) \\ V_{gc}(k+1) \end{bmatrix} = B(\sigma) \begin{bmatrix} V_{ga}(k) \\ V_{gb}(k) \\ V_{gc}(k) \end{bmatrix} \tag{26}$$

where

$$B(\sigma) = \frac{2}{3} \begin{bmatrix} \cos(\sigma) & -\frac{1}{2}\cos(\sigma - \frac{\pi}{3}) & -\frac{1}{2}\cos(\sigma + \frac{\pi}{3}) \\ -\frac{1}{2}\cos(\sigma + \frac{\pi}{3}) & \cos(\sigma) & -\frac{1}{2}\cos(\sigma - \frac{\pi}{3}) \\ -\frac{1}{2}\cos(\sigma - \frac{\pi}{3}) & -\frac{1}{2}\cos(\sigma + \frac{\pi}{3}) & \cos(\sigma) \end{bmatrix}$$

σ is equal to ωT_s and ω is the grid angular frequency. The predicted results at $(k+1)$ sample are then used by the MMPC+B&B algorithm to estimate the optimal switching duty ratio at the $(k+2)$th sample, which can minimize the cost function given as follows:

$$J(k) = \sum_{m=a,b,c} \left\{ \left(I_{\text{cm}}(k+2) - I^*_{\text{cm}}(k+2) \right)^2 \right\} + \lambda \sum_{m=a,b,c} \left\{ \left(V^{\Sigma}_m(k+2) - V^{\Sigma *}_m(k+2) \right)^2 \right\}$$

$$\text{s.t.} \; |S_m(k+1)| \leq 1. \tag{27}$$

V. EXPERIMENTAL TESTS AND RESULTS

A. Experimental Setup

To validate and demonstrate the performance of the proposed MMPC+B&B control scheme, experimental tests were conducted on an MMCC-STATCOM prototype (see Fig. 5) built at the Smart Grid Laboratory of the University of Leeds. The configuration of the power network model constructed for testing the STATCOM's capability for unbalanced current cancellation is as given in Fig. 1, the PCC bus is powered by an auto transformer (3 kVA,110 V) through a three-phase *RL* element imitating the transmission line impedance. The parameters of the main components in the experimental setup are listed in Table V.

The experimental MMCC-STATCOM rig is comprised of six SMs, each being a full-bridge 5L-flying capacitor converter consisting of three-capacitors and eight IGBT-Diode pairs. Two of SMs are connected in series per phase, giving nine voltage levels. The digital device for the control unit is a combination of an ACTEL-Pro-Asic three FPGA module and a Texas Instrument 32-bit floating point digital-signal-processor (DSP-TMS320C6713). The DSP serves as the main control unit for processing all measured data to execute MMPC+B&B control algorithm while the FPGA implements the PS-PWM scheme. The resultant switching signals are supplied to the SMs through fiber optic transmitter and receiver circuits.

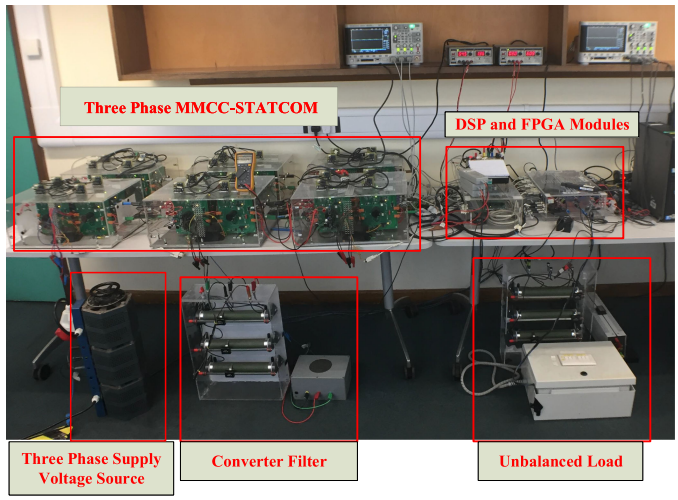

Fig. 6. MMCC-STATCOM prototype and other system hardware components.

B. Results and Discussions

Figs. 7 and 8 show the experimental results when the proposed scheme is applied to control the experimental MMCC-STATCOM, the former has the weighting factor λ setting to 0.25 and the latter as 0.49. Fig. 9 shows the corresponding waveforms when the conventional sinusoidal zero-sequence voltage injection is applied to the same experimental rig. In all the three figures, stepped lines plotted in (a) depict the levels of compensation ratio to the imbalanced load current. In this article, the unbalanced load current is fixed at K_{ir}=I^- /I^+=0.7. The unbalance compensation ratio is adjusted from 0% (between 0.0 s and 0.1 s) up to 70% at the step size of 14% per 0.1 s. Thus, in the initial period of 0 to 0.1 s, the PCC current is unbalanced since there is no compensation. After 0.1 s the degree of compensation is increased gradually. The PCC currents become more balanced until the maximum 70% compensation is applied. The unbalanced compensation ratio at 0.7 is maintained from 0.5 to 0.7 s in order to observe the level of voltage oscillations away around the average SM capacitor voltages.

The performance of MMPC+B&B algorithm can be observed from the PCC current waveforms shown in Figs. 7(b) and 8(b). From no compensation applied (0 s to 0.1 s) to 70% of current imbalance compensation, it is evident that the degree of PCC current imbalance is reduced gradually to near complete elimination during period 0.5 s to 0.7 s. The three-phase current waveforms supplied by MMCC to the grid are displayed in Figs. 7(c) and 8(c), it can be seen that the degree of converter current imbalance increases with the escalation of the required level of compensation, but they are all within the rated limit. Likewise the terminal phase voltages of the MMCC are also within the rated level without over modulation. Figs. 7(e) and 8(e) display the three-phase SMs capacitor average voltages,

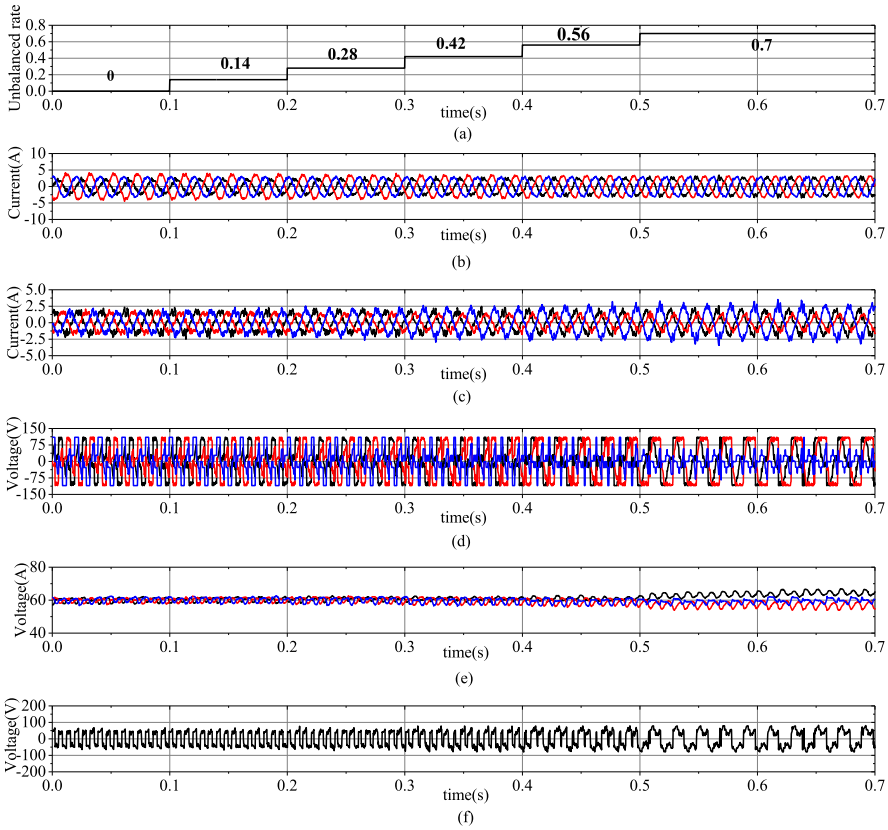

Fig. 7. Experimental results (a) Unbalanced rate. (b) PCC current. (c) Output converter current. (d) Converter terminal voltage. (e) Sub-modules' capacitor voltages for each phase. (f) Common mode voltage for proposed method when $\lambda = 0.25$.

which are well balanced even when the compensation level is set to 56%, low-voltage fluctuation with peak–peak value about 6 V (10% of rated capacitor voltage) is shown before time instant 0.5 s. Voltage deviations grow slightly during the final 0.2 s interval when the compensation level is as high as 70%. However, the adverse effect of this condition to the control performance is minimal, the system still maintains stable operation with PCC current being well balanced.

It is worth noting that weighting factor value affects performance of compensation. When the weighting factor is 0.49, the degree of capacitor voltages deviation is lower than that when the value is 0.25. However, for the reduced weighting factor, the performance in unbalanced current compensation is better. When weighting factor is 0.49, the maximum difference between the peak values of the three PCC phase currents is about 0.5 A, higher than that with the weighting factor being 0.25 which is 0.3 A. This means that the unbalanced ratio after compensation is higher than its counterpart when the weighting factor is 0.49. In terms of CMV (zero-sequence voltage), as shown in Figs. 7(f) and 8(f), the peak values for both cases are always around 60 V, so none presents the overmodulation problem.

The above-mentioned results are compared with those shown in Fig. 9 where the conventional method using zero-sequence voltage injection for intercluster voltage balance is applied. In this case to extend the MMCC STATCOM voltage range, the zero-sequence voltage injected is composed of a sinusoidal fundamental element plus two third harmonics; one has the magnitude of one-sixth of its main fundamental component and the other's magnitude is one-sixth of the positive sequence component of the converter terminal voltage.

As can be seen, the waveforms up to $t = 0.5$ s when the compensation ratio is 0.56 (see Figs. 7–9) are stable for both methods. However, as load imbalance compensation ratio is increased to a higher level of 0.7, the performance of the controlled PCC current waveforms from the conventional method deteriorates, as shown in Fig. 9(b). This is due to increasing the negative sequence current for mitigating load imbalance, adversely increases phase active power imbalance. However, the zero-sequence voltage injected is insufficient to eliminate the phase power differences even though the magnitude of its fundamental element has increased significantly [see Fig. 9(f)]. Consequently, the phase voltages drift away from their nominal levels as seen in Fig. 9(e), resulting in system becomes uncontrollable. In contrast, the results from the proposed control scheme, depicting in Figs. 7 and 8, show that the CMV magnitude does not show noticeable increment but its spectra changes significantly for eliminating phase power imbalance. This, in turn, prevents the phase voltages drifting apart, hence, enables effective cancellation of the unbalanced load current. Thus, the proposed MMPC has shown that it allows the STATCOM compensating higher level of load unbalance compared to the conventional method.

To explore the advantage of the MMPC+B&B algorithm, the frequency spectra of the CMVs derived by FFT analysis are

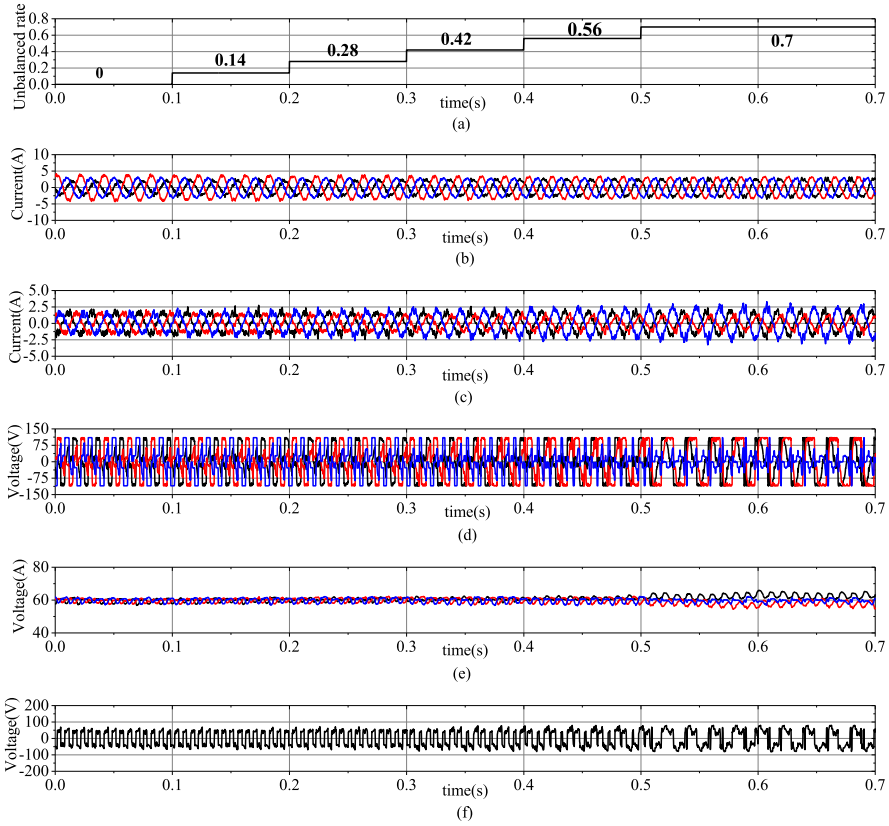

Fig. 8. Experimental results (a) Unbalanced rate. (b) PCC current. (c) Output converter current. (d) Converter terminal voltage. (e) Sub-modules' capacitor voltages for each phase. (f) Common mode voltage for proposed method when $\lambda = 0.49$.

compared as shown in Figs. 10 and 11 when unbalanced ratio is set to 0.42. It can be seen clearly from Fig. 10(a) and (b) that the odd harmonics dominate the other frequency components. In particular, the magnitude of the third harmonic exceeds that of the fundamental element, and other odd harmonics, for example, when $\lambda = 0.25$, fifth- and seventh-order harmonics are about 40% and 75% of the fundamental, respectively. For $\lambda = 0.49$, there are about 35% of fifth and 70% of seventh harmonics existing in CMV waveform. In contrast, the dominate components in the zero-sequence voltage obtained from the conventional method (see Fig. 11) are only the fundamental and third harmonic elements, with the magnitude of the third harmonic being below 40% of the fundamental frequency. This confirms that the proposed method is capable of making use of the harmonic components for power balance between phases hence achieving a superior performance for unbalanced current mitigation. Furthermore, the peak amplitude of the fundamental element in CMV for the period between 0.3 and 0.4 s is as low as 27.42 V when $\lambda = 0.25$ and that for $\lambda = 0.49$ is 29.34 V, whereas for the conventional method, the magnitude is a lot higher reaching 40.35 V; hence, the proposed method offers a higher level of unbalanced current compensation without pushing the MMCC terminal voltages into over modulation range.

C. Weighting Factor Selection

As stated the weighting factor, λ, is determined by trial and error depending on the requirements to converter current control accuracy, according to the PCC current THD factor, the levels of the three-phase capacitor voltage deviations, and the voltage ripple percentages. It is clear that setting a higher weighting factor imposes a tighter limit on voltage deviation levels while compromising the PCC current control performance, hence resulting in its THD value being increased. Conversely, a lower weighting factor would result in better current control, and hence, lower PCC phase current THD values, but the constraints on phase voltage deviations are weakened. With high-phase voltage deviations reaching the extent that one phase voltage drifts away, the system will become uncontrollable.

TABLE VI
RESULTS FOR DIFFERENT WEIGHTING FACTORS

Weighting factor	PCC current THD	Sub-module capacitor voltage ripple percentage	Sub-module capacitor voltage deviation
0.81	3.57%	7.7%	0.74V
0.64	3.52%	8%	1.11V
0.49	3.48%	8.4%	1.66V
0.36	3.31%	9.3%	3.23V
0.25	3.2%	9.5%	5.26V
0.16	3.14%	10.2%	Out of Range
0.09	3.08%	10.5%	Out of Range

To demonstrate clearly the effect of λ on the control of PCC current and SM capacitor voltage balance, a test was performed on the MPC control scheme, for the STATCOM operating under the unbalanced PCC current condition. λ varies from low at 0.016 to high at 0.81 with step size 0.1. Table VI lists the corresponding PCC current THD values, the maximum voltage

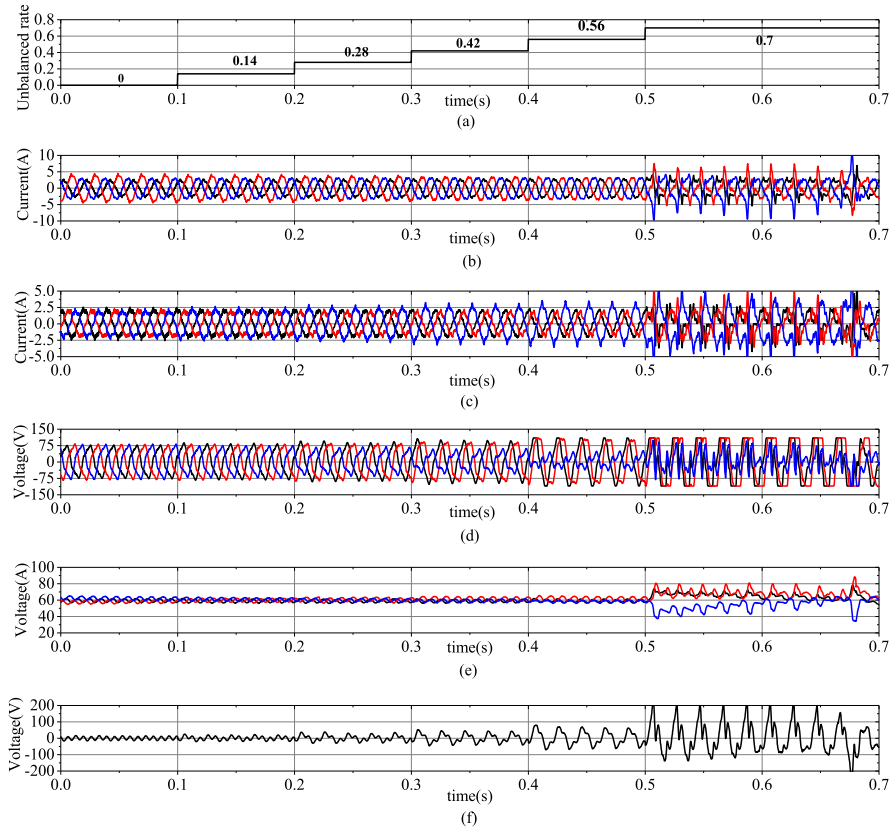

Fig. 9. Experimental results (a) Unbalanced rate. (b) PCC current. (c) Output converter current. (d) Converter terminal voltage. (e) Sub-modules' capacitor voltages for each phase. (f) Common mode voltage for conventional zero sequence voltage injection method.

ripple percentages, and the differences between the summed SM capacitor voltages per phase.

Clearly at high λ (0.81), the PCC current THD value is higher at 3.57% while the SM capacitor voltage ripple is the lowest at 7.7% and the voltage deviation is low (0.74 V). As λ decreases, control on the PCC current improves with steadily reducing THD values. However, the SM capacitor voltage balance control is weakened, causing increases in both the SM capacitor percentage voltage ripples and phase voltage deviations. As λ is reduced further to 0.16, the three-phase capacitor voltages cannot be maintained at the balanced levels. As shown in Fig. 12, the three-phase voltages drift continuously in different directions, so that one phase voltage pushes the MMC STATCOM into the overmodulation range. This is referred to as "out of range" in Table VI since the sum of the capacitor voltages in one phase leg becomes higher than the maximum allowed value (80 V).

Fig. 13(a) and (b) shows the variations of the sums of SM capacitor voltages with λ=0.25 and 0.49, respectively. For both cases, the compensation ratio is 70% and the time of test is from 0 s to 0.9 s. It can be seen clearly that there is no occurrence of uncontrolled phase voltage drift in either cases. However, with the λ value of 0.25, the differences of the summed phase capacitor voltages differences are larger, which implies a weaker voltage balance control performance. After repeated tests the proposed λ value = 0.49 is chosen as good compromise between maintaining balance of the summed SM capacitor voltages and giving good current control performance with a low enough THD value.

VI. Conclusion

This article presented a new MMPC scheme for an MMCC-STATCOM, shunt connected to the PCC bus of a power grid, to eliminate the unbalanced current and improve the power factor. The proposed method employs a modified B&B algorithm to select the optimal switch duty ratios for the converter. The current and capacitor voltage prediction models are presented together with the cost function and constraint. The procedures for B&B algorithm implementation were described in detail. Experimental validations of the proposed control scheme were performed. The results obtained demonstrated superior performance as compared to the traditional sinusoidal zero sequence waveform injection method. The distinctive features of this new method can be summarized as follows.

1) Injecting a CMV in the phase voltages of a STAR-connected MMCC reduces the peak phase voltages, hence, extends the unbalanced load current compensation range up to 70%, whereas the conventional method can only reach 60%.
2) The proposed method is experimentally verified that good performance in unbalanced current and reactive current cancellation with the compensation current below the rated limit.
3) The SM capacitor voltages can be well balanced, achieving significant reduction of the capacitor voltage ripples down to 8.0% compared with 10% for the conventional scheme under the same operation conditions.

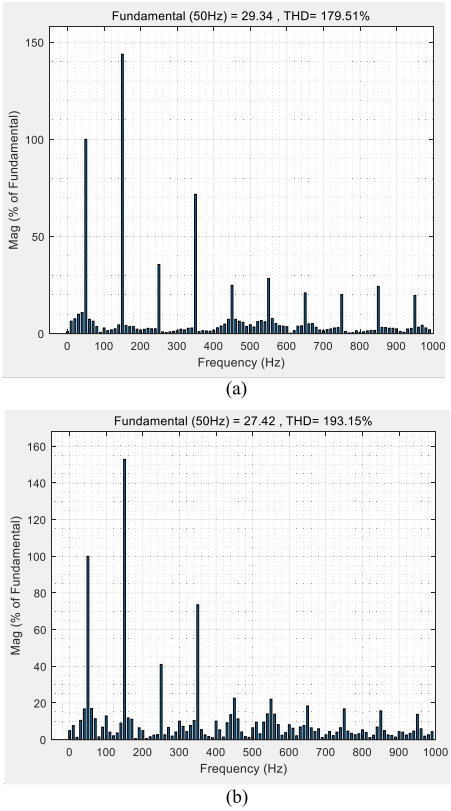

Fig. 10. Frequency spectra of CMV when unbalanced ratio is 0.42 for (a) proposed method with $\lambda = 0.25$ and (b) proposed method with $\lambda = 0.49$.

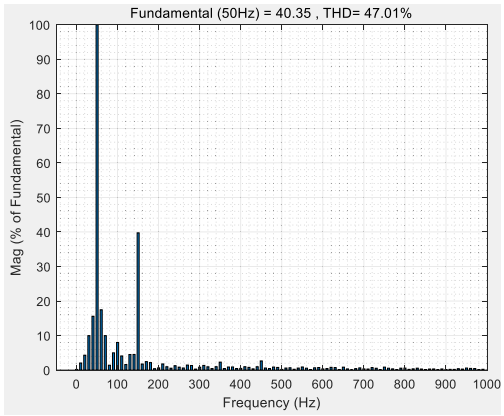

Fig. 11. Frequency spectra of CMV when unbalanced ratio is 0.42 for conventional method.

APPENDIX

$$c_2 = -\frac{1}{3}\frac{T_s}{L_f}V_b^{\Sigma}(k)$$

$$b_1 = c_1 = -\frac{1}{3}\frac{T_s}{L_f}V_a^{\Sigma}(k), b_2 = \frac{2}{3}\frac{T_s}{L_f}V_b^{\Sigma}(k)$$

$$b_3 = -\frac{1}{3}\frac{T_s}{L_f}V_c^{\Sigma}(k), c_3 = \frac{2}{3}\frac{T_s}{L_f}V_c^{\Sigma}(k)$$

$$b_4 = -\frac{T_s}{C}I_{cb}(k), c_4 = -\frac{T_s}{C}I_{cc}(k)$$

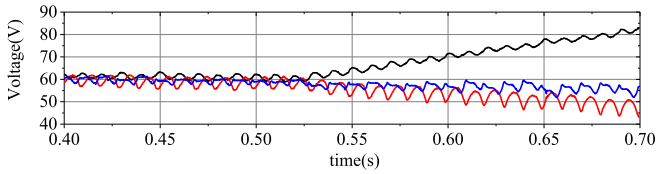

Fig. 12. Variations of the sum of SMs capacitor voltages with λ=0.16 and compensation ratio 70%.

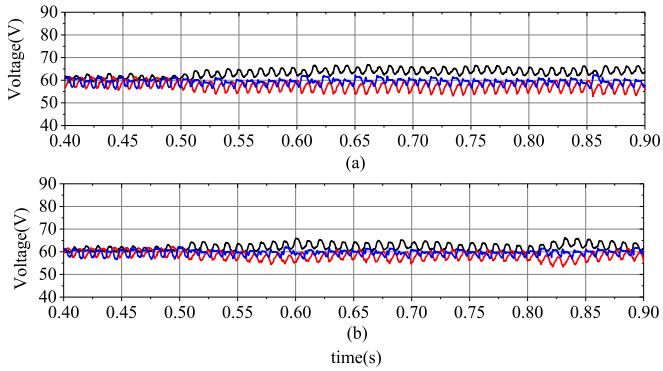

Fig. 13. Variations of the sum of SMs capacitor voltages with (a) $\lambda = 0.25$ and (b) $\lambda = 0.49$ when the compensation ratio is 70%.

$$n_{b1} = -\frac{1}{3}\frac{T_s}{L_f}V_c^{\Sigma}(k)S_c(k) - \frac{T_s}{L_f}V_{gb}(k) + \left(1 - \frac{R_f T_s}{L_f}\right)I_{cb}(k) - I_{cb}^*(k+1)$$

$$n_{c1} = -\frac{1}{3}\frac{T_s}{L_f}V_c^{\Sigma}(k)S_c(k) - \frac{T_s}{L_f}V_{gc}(k) + \left(1 - \frac{R_f T_s}{L_f}\right)I_{cc}(k) - I_{cc}^*(k+1)$$

$$n_{b2} = P_{b2} = V_b^{\Sigma}(k) - V_b^{\Sigma *}(k+1)$$

$$n_{c2} = P_{c2} = V_c^{\Sigma}(k) - V_c^{\Sigma *}(k+1)$$

$$P_{b1} = -\frac{T_s}{L_f}V_{gb}(k) + \left(1 - \frac{R_f T_s}{L_f}\right)I_{cb}(k) - I_{cb}^*(k+1)$$

$$P_{c1} = -\frac{T_s}{L_f}V_{gc}(k) + \left(1 - \frac{R_f T_s}{L_f}\right)I_{cc}(k) - I_{cc}^*(k+1)$$

$$n_{a3} = \frac{2}{3}\frac{T_s}{L_f}V_a^{\Sigma}(k)S_a(k) - \frac{1}{3}\frac{T_s}{L_f}V_b^{\Sigma}(k)S_b(k) - \frac{T_s}{L_f}V_{ga}(k) + \left(1 - \frac{R_f T_s}{L_f}\right)I_{ca}(k) - I_{ca}^*(k+1)$$

$$n_{b3} = -\frac{1}{3}\frac{T_s}{L_f}V_a^{\Sigma}(k)S_a(k) + \frac{2}{3}\frac{T_s}{L_f}V_b^{\Sigma}(k)S_b(k) - \frac{T_s}{L_f}V_{gb}(k) + \left(1 - \frac{R_f T_s}{L_f}\right)I_{cb}(k) - I_{cb}^*(k+1)$$

$$n_{c3} = -\frac{1}{3}\frac{T_s}{L_f}V_a^{\Sigma}(k)S_a(k) - \frac{1}{3}\frac{T_s}{L_f}V_b^{\Sigma}(k)S_b(k) - \frac{T_s}{L_f}V_{gc}(k) + \left(1 - \frac{R_f T_s}{L_f}\right)I_{cc}(k) - I_{cc}^*(k+1).$$

REFERENCES

[1] M. Eremia, C.-C. Liu, and A.-A. Edris, *Advanced Solutions in Power Systems: HVdc, FACTS, and Artificial Intelligence*. Hoboken, NJ, USA: Wiley, 2016.

[2] L. Wang, C.-S. Lam, and M.-C. Wong, "A hybrid-STATCOM with wide compensation range and low DC-link voltage," *IEEE Trans. Ind. Electron.*, vol. 63, no. 6, pp. 3333–3343, Jun. 2016.

[3] K. Mahapatra, A. Ghosh, and S. Doradla, "Simplified model for control design of statcom using three-level inverter," in *Proc. IEEE TENCON'98. IEEE Region 10 Int. Conf. Glob. Connectivity Energy, Comput., Commun. Control*, 1998, vol. 2, pp. 536–539.

[4] M. Hagiwara and H. Akagi, "Control and experiment of pulsewidth-modulated modular multilevel converters," *IEEE Trans. Power Electron.*, vol. 24, no. 7, pp. 1737–1746, Jul. 2009.

[5] S. Debnath, J. Qin, B. Bahrani, M. Saeedifard, and P. Barbosa, "Operation, control, and applications of the modular multilevel converter: A review," *IEEE Trans. Power Electron.*, vol. 30, no. 1, pp. 37–53, Jan. 2015.

[6] H. Akagi, "Classification, terminology, and application of the modular multilevel cascade converter (MMCC)," *IEEE Trans. Power Electron.*, vol. 26, no. 11, pp. 3119–3130, Nov. 2011.

[7] Y. Yu, G. Konstantinou, B. Hredzak, and V. G. Agelidis, "Power balance of cascaded H-bridge multilevel converters for large-scale photovoltaic integration," *IEEE Trans. Power Electron.*, vol. 31, no. 1, pp. 292–303, Feb. 2016.

[8] A. Stillwell, E. Candan, and R. C. Pilawa-Podgurski, "Active voltage balancing in flying capacitor multi-level converters with valley current detection and constant effective duty cycle control," *IEEE Trans. Power Electron.*, vol. 34, no. 11, pp. 11429–11441, Nov. 2019.

[9] X. Xing, X. Li, F. Gao, C. Qin, and C. Zhang, "Improved space vector modulation technique for neutral-point voltage oscillation and common-mode voltage reduction in three-level inverter," *IEEE Trans. Power Electron.*, vol. 34, no. 9, pp. 8697–8714, Sep. 2019.

[10] X. Xing, Z. Zhang, C. Zhang, J. He, and A. Chen, "Space vector modulation for circulating current suppression using deadbeat control strategy in parallel three-level neutral-clamped inverters," *IEEE Trans. Ind. Electron.*, vol. 64, no. 2, pp. 977–987, Feb. 2017.

[11] S. Kouro *et al.*, "Recent advances and industrial applications of multilevel converters," *IEEE Trans. Ind. Electron.*, vol. 57, no. 8, pp. 2553–2580, Aug. 2010.

[12] Y. Li and B. Wu, "A novel DC voltage detection technique in the CHB inverter-based STATCOM," *IEEE Trans. Power Del.*, vol. 23, no. 3, pp. 1613–1619, Jul. 2008.

[13] J. A. Barrena, L. Marroyo, M. Á. R. Vidal, and J. R. T. Apraiz, "Individual voltage balancing strategy for PWM cascaded h-bridge converter-based STATCOM," *IEEE Trans. Ind. Electron.*, vol. 55, no. 1, pp. 21–29, Jan. 2008.

[14] Z. Liu, B. Liu, S. Duan, and Y. Kang, "A novel DC capacitor voltage balance control method for cascade multilevel STATCOM," *IEEE Trans. Power Electron.*, vol. 27, no. 1, pp. 14–27, Jan. 2012.

[15] H. Akagi, S. Inoue, and T. Yoshii, "Control and performance of a transformerless cascade PWM STATCOM with STAR configuration," *IEEE Trans. Ind. Appl.*, vol. 43, no. 4, pp. 1041–1049, Jul./Aug. 2007.

[16] C. Han, A. Q. Huang, Y. Liu, and B. Chen, "A generalized control strategy of per-phase DC voltage balancing for cascaded multilevel converter-based STATCOM," in *Proc. IEEE Power Electron. Specialists Conf.*, 2007, pp. 1746–1752.

[17] L. Maharjan, S. Inoue, and H. Akagi, "A transformerless energy storage system based on a cascade multilevel PWM converter with STAR configuration," *IEEE Trans. Ind. Appl.*, vol. 44, no. 5, pp. 1621–1630, Sep./Oct. 2008.

[18] R. Betz, T. Summers, and T. Furney, "Symmetry compensation using a H-bridge multilevel STATCOM with zero sequence injection," in *Conf. Rec. IEEE Ind. Appl. Conf. 41st IAS Annu. Meeting*, 2006, vol. 4, pp. 1724–1731.

[19] Q. Song and W. Liu, "Control of a cascade STATCOM with STAR configuration under unbalanced conditions," *IEEE Trans. Power Electron.*, vol. 24, no. 1, pp. 45–58, Jan. 2009.

[20] L. Maharjan, S. Inoue, H. Akagi, and J. Asakura, "State-of-charge (SoC)-balancing control of a battery energy storage system based on a cascade PWM converter," *IEEE Trans. Power Electron.*, vol. 24, no. 6, pp. 1628–1636, Jun. 2009.

[21] J. I. Y. Ota, Y. Shibano, N. Niimura, and H. Akagi, "A phase-shifted-PWM D-STATCOM using a modular multilevel cascade converter (SSBC)—Part I: Modeling, analysis, and design of current control," *IEEE Trans. Ind. Appl.*, vol. 51, no. 1, pp. 279–288, Jan./Feb. 2015.

[22] J. I. Y. Ota, Y. Shibano, and H. Akagi, "A phase-shifted PWM D-STATCOM using a modular multilevel cascade converter (SSBC)—Part II: Zero-voltage-ride-through capability," *IEEE Trans. Ind. Appl.*, vol. 51, no. 1, pp. 289–296, Jan./Feb. 2015.

[23] O. J. Oghorada and L. Zhang, "Unbalanced and reactive load compensation using MMCC-based STATCOMS with third-harmonic injection," *IEEE Trans. Ind. Electron.*, vol. 66, no. 4, pp. 2891–2902, Apr. 2019.

[24] S.-F. Chou *et al.*, "Average power balancing control of a STATCOM based on the cascaded H-bridge PWM converter with STAR configuration," in *Proc. IEEE Energy Convers. Congr. Expo.*, 2013, pp. 970–977.

[25] L. Zhao, S. Yan-Jun, D. Shan-Xu, K. Yong, and C. Tian-Jin, "The research of DC capacitance voltages balancing strategy based on cascade STATCOM using individual phase instantaneous current tracking," in *Proc. IEEE 6th Int. Power Electron. Motion Control Conf.*, 2009, pp. 1136–1140.

[26] R. E. Betz, T. J. Summers, and B. J. Cook, "Outline of the control design for a cascaded H-bridge STATCOM," in *Proc. IEEE Ind. Appl. Soc. Annu. Meeting*, 2008, pp. 1–8.

[27] N. Hatano and T. Ise, "Control scheme of cascaded H-bridge STATCOM using zero-sequence voltage and negative-sequence current," *IEEE Trans. Power Del.*, vol. 25, no. 2, pp. 543–550, Apr. 2010.

[28] J. Qin and M. Saeedifard, "Predictive control of a modular multilevel converter for a back-to-back HVdc system," *IEEE Trans. Power Del.*, vol. 27, no. 3, pp. 1538–1547, Jul. 2012.

[29] M. Vatani, B. Bahrani, M. Saeedifard, and M. Hovd, "Indirect finite control set model predictive control of modular multilevel converters," *IEEE Trans. Smart Grid*, vol. 6, no. 3, pp. 1520–1529, May 2015.

[30] P. Liu, Y. Wang, W. Cong, and W. Lei, "Grouping-sorting-optimized model predictive control for modular multilevel converter with reduced computational load," *IEEE Trans. Power Electron.*, vol. 31, no. 3, pp. 1896–1907, Mar. 2016.

[31] A. Dekka, B. Wu, V. Yaramasu, and N. R. Zargari, "Dual-stage model predictive control with improved harmonic performance for modular multilevel converter," *IEEE Trans. Ind. Electron.*, vol. 63, no. 10, pp. 6010–6019, Oct. 2016.

[32] J.-W. Moon, J.-S. Gwon, J.-W. Park, D.-W. Kang, and J.-M. Kim, "Model predictive control with a reduced number of considered states in a modular multilevel converter for HVdc system," *IEEE Trans. Power Del.*, vol. 30, no. 2, pp. 608–617, Apr. 2015.

[33] A. Dekka, B. Wu, V. Yaramasu, and N. R. Zargari, "Model predictive control with common-mode voltage injection for modular multilevel converter," *IEEE Trans. Power Electron.*, vol. 32, no. 3, pp. 1767–1778, Mar. 2017.

[34] Z. He, P. Guo, Z. Shuai, Q. Xu, A. Luo, and J. M. Guerrero, "Modulated model predictive control for modular multilevel AC/AC converter," *IEEE Trans. Power Electron.*, vol. 34, no. 10, pp. 10359–10372, Oct. 2019.

[35] D. Zhou, S. Yang, and Y. Tang, "Model-predictive current control of modular multilevel converters with phase-shifted pulsewidth modulation," *IEEE Trans. Ind. Electron.*, vol. 66, no. 6, pp. 4368–4378, Jun. 2019.

[36] Z. Gong, X. Wu, P. Dai, and R. Zhu, "Modulated model predictive control for MMC-based active front-end rectifiers under unbalanced grid conditions," *IEEE Trans. Ind. Electron.*, vol. 66, no. 3, pp. 2398–2409, Mar. 2019.

[37] E. Fuentes, C. A. Silva, and R. M. Kennel, "MPC implementation of a quasi-time-optimal speed control for a PMSM drive, with inner modulated-FS-MPC torque control," *IEEE Trans. Ind. Electron.*, vol. 63, no. 6, pp. 3897–3905, Jun. 2016.

[38] J. Xu *et al.*, "Carrier-based modulated model predictive control strategy for three-phase two-level VSIS," *IEEE Trans. Energy Convers.*, vol. 36, no. 3, pp. 1673–1687, Sep. 2021.

[39] J. Wang, X. Liu, Q. Xiao, D. Zhou, H. Qiu, and Y. Tang, "Modulated model predictive control for modular multilevel converters with easy implementation and enhanced steady-state performance," *IEEE Trans. Power Electron.*, vol. 35, no. 9, pp. 9107–9118, Sep. 2020.

[40] Y. Zhang, X. Wu, and X. Yuan, "A simplified branch and bound approach for model predictive control of multilevel cascaded H-bridge STATCOM," *IEEE Trans. Ind. Electron.*, vol. 64, no. 10, pp. 7634–7644, Oct. 2017.

[41] Y. Zhang, X. Yuan, X. Wu, Y. Yuan, and J. Zhou, "Parallel implementation of model predictive control for multilevel cascaded H-bridge STATCOM with linear complexity," *IEEE Trans. Ind. Electron.*, vol. 67, no. 2, pp. 832–841, Feb. 2020.

[42] Y. Zhang, X. Wu, X. Yuan, Y. Wang, and P. Dai, "Fast model predictive control for multilevel cascaded H-bridge STATCOM with polynomial computation time," *IEEE Trans. Ind. Electron.*, vol. 63, no. 8, pp. 5231–5243, Aug. 2016.

[43] J. Yin, J. I. Leon, M. A. Perez, L. G. Franquelo, A. Marquez, and S. Vazquez, "Model predictive control of modular multilevel converters using quadratic programming," *IEEE Trans. Power Electron.*, vol. 36, no. 6, pp. 7012–7025, Jun. 2021.
[44] R. K. Sundaram, "Inequality constraints and the theorem of Kuhn and Tucker," in *A First Course in Optimization Theory*. New York, NY, USA: Cambridge Univ. Press, 1996, pp. 145–171.
[45] A. Shustrova, *Primal-Dual Interior Methods for Quadratic Programming*. San Diego, CA, USA: Univ. Calif., 2015.
[46] J. A. Momoh, S. Guo, E. Ogbuobiri, and R. Adapa, "The quadratic interior point method solving power system optimization problems," *IEEE Trans. Power Syst.*, vol. 9, no. 3, pp. 1327–1336, Aug. 1994.
[47] C. Feng, J. Liang, and V. G. Agelidis, "Modified phase-shifted PWM control for flying capacitor multilevel converters," *IEEE Trans. Power Electron.*, vol. 22, no. 1, pp. 178–185, Jan. 2007.
[48] P. Rodríguez, J. Pou, J. Bergas, J. I. Candela, R. P. Burgos, and D. Boroyevich, "Decoupled double synchronous reference frame PLL for power converters control," *IEEE Trans. Power Electron.*, vol. 22, no. 2, pp. 584–592, Mar. 2007.

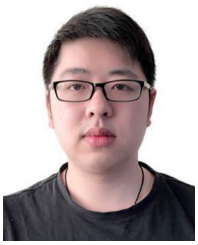

Xuejiao Pan was born in Wuxi, Jiangsu, China, in 1994. He received the B.Eng. degree in electrical engineering from Nantong University, Nantong, China, in 2016, and the M.Sc. degree in electronic/electrical engineering in 2018 from the University of Leeds, Leeds, U.K., where he is currently working toward the Ph.D. degree in electronic/electrical engineering.

His research interests include modulation and control of power converters, multilevel converters, modular multilevel converters, FACTs devices, and harmonic cancellation methods.

Li Zhang (Senior Member, IEEE) received the Ph.D. degree in control engineering from Bradford University, Bradford, U.K., in 1985.

He was a Research Fellow with Oxford University, Oxford, U.K. She was then a Lecturer with the University of Bradford, Bradford, U.K., and is currently a Senior Lecturer with the School of Electronic and Electrical Engineering, University of Leeds, Leeds, U.K. He has been an Adjunct Professor with Chongqing University, Chongqing, China, since 2006, and Joint Grant holder of China State Natural Science Foundation Fund (60712, 2014 01-2017 12) entitled: Analysis and research on the hotspot effect and its control method of the photovolaic system. She has authored and coauthored more than 130 technical papers in the fields of power electronics, renewable power generation system, and wind generator control, and three books on power converter circuits and wind power electricity generation.

Dr. Zhang is currently an Associate Editor for the IEEE TRANSACTION ON POWER ELECTRONICS and was also the Associate Editor for *IET proceedings on Power Electronics* between 2014 and 2017.

Yongfei Li was born in Henan, China, in 1995. He received the B.Eng. degree in electrical engineering in 2016 from the Harbin Institute of Technology, Harbin, China, where he is currently working toward the Ph.D. degree with the Department of Electrical Engineering.

His research interests include PMSMs, special motors, and motor control.

Kang Li (Senior Member, IEEE) received the B.Sc. degree in industrial automation from Xiangtan University, Hunan, China, in 1989, the M.Sc. degree in control theory and applications from the Harbin Institute of Technology, Harbin, China, in 1992, the Ph.D. degree in control theory and applications from Shanghai Jiaotong University, Shanghai, China, in 1995, and the D.Sc. degree in engineering from Queen's University Belfast, Belfast, U.K., in 2015.

Between 1995 and 2002, he was with Shanghai Jiaotong University, Shanghai, China, Delft University of Technology, Delft, The Netherlands, and Queen's University Belfast, Belfast, U.K., as a Research Fellow. Between 2002 and 2018, he was a Lecturer in 2002, a Senior Lecturer in 2007, a Reader in 2009, and a Chair Professor in 2011 with the School of Electronics, Electrical Engineering and Computer Science, Queen's University Belfast, Belfast, U.K. He currently holds the Chair of Smart Energy Systems with the University of Leeds, Leeds, U.K. His research interests cover nonlinear system modeling, identification, and control, and machine learning, with substantial applications to energy and power systems, smart grid, transport decarbonization, and energy management in energy intensive manufacturing processes. He has authored/coauthored more than 200 journal publications and edited/coedited 18 conference proceedings. He is also a Visiting Professor of Shanghai Jiaotong University, Shanghai, China, Southeast University, Dhaka, Bangladesh, Tianjin University, Tianjin, China, Shanghai University, Shanghai, China, and Xiangtan University, Xiangtan, China.

Dr. Li was the Chair of the IEEE UKRI Control and Communication Ireland chapter, the Secretary of the IEEE U.K., and Ireland Section and was the recipient of more than 20 prizes and awards, including a recent Springer Nature "China New Development Award" in 2019 in recognition of the "exceptional contributions to the delivery of the UN Sustainable Development Goals."

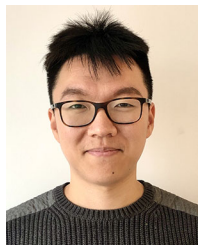

Han Huang (Member, IEEE) received the Ph.D. degree in electronic and electrical engineering from the University of Leeds, Leeds, U.K., in 2019.

He was a Postdoctoral Researcher with Energy Safety Research Institute, Swansea University, Swansea, U.K. In 2021, he joined the HVdc Centre of Excellence, GE's Grid Solutions, Stafford, U.K., as a Lead Electrical Engineer. His research interests include modular multilevel converter control, HVdc system design, FACTs, and integration of renewable energies into the power grid.